Title

Demonstration of Photovoltaic Action and Enhanced Stability from a Quasi-Two-Dimensional Hybrid Organic—Inorganic Copper–Halide Material Incorporating Divalent Organic Groups

Journal

ACS Applied Energy Materials, 2(3)

ISSN

2574-0962

Authors

Fabian, David M
Ziller, Joseph W
Solis-Ibarra, Diego
et al.

Publication Date

2019-03-25

DOI

10.1021/acsaem.8b02134

ACS APPLIED ENERGY MATERIALS

Article

Cite This: ACS Appl. Energy Mater. 2019, 2, 2178−2187

www.acsaem.org

Demonstration of Photovoltaic Action and Enhanced Stability from a Quasi-Two-Dimensional Hybrid Organic−Inorganic Copper−Halide Material Incorporating Divalent Organic Groups

David M. Fabian,[†] Joseph W. Ziller,[†] Diego Solis-Ibarra,[‖] and Shane Ardo*[,†,§,‡]

[†]Department of Chemistry, [§]Department of Materials Science & Engineering, and [‡]Department of Chemical & Biomolecular Engineering, University of California, Irvine, Irvine, California 92697-2025, United States

[‖]Instituto de Investigaciones en Materiales, Universidad Nacional Autónoma de México, CU, Coyoacán, 04510, Ciudad de México México

Supporting Information

ABSTRACT: Commercialization of solar cells based on photoactive lead halide perovskites is in part limited by their toxicity and instability. In this study, new and related copper halide hybrid organic−inorganic materials containing dicationic hexane-1,6-diammonium ($^{+}H_3N-C_6H_{12}-NH_3^{+}$) demonstrated superior stability to heat and moisture in comparison to the analogous material containing monocationic *n*-propylammonium ($C_3H_7-NH_3^{+}$) in twice the stoichiometry. Electronic absorption spectra taken of the materials were consistent with an indirect optical bandgap of ∼1.8 eV, making them well-suited for application as the photoactive layer in the top cell of a tandem solar cell with silicon. The best-performing single-junction solar cells containing the dicationic material as the photoactive layer exhibited an open-circuit photovoltage in excess of 400 mV and a short-circuit photocurrent density of ∼30 $\mu A/cm^2$. These values are similar to those reported for state-of-the-art copper halide hybrid organic−inorganic materials containing organic monocations and motivate further research on this class of materials.

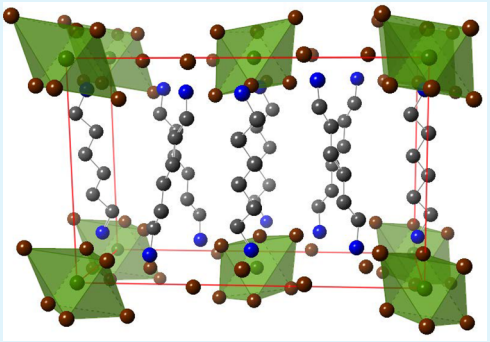

KEYWORDS: *solar cell, photovoltaic, perovskite, two-dimensional material, copper halide, hybrid material, stability, dications*

INTRODUCTION

Photoactive hybrid organic−inorganic lead halide perovskite ($APbX_3$) materials can be fabricated into >20% efficient thin-film solar cells.[1−5] These materials also have tunable bandgaps, which allow them to serve as light-absorbers in single-junction solar cells or in the top cell of a tandem solar cell with silicon.[6,7] However, $APbX_3$ materials incorporate toxic lead and are extremely unstable to moisture and heat, even under ambient conditions,[8−10] suggesting that challenges remain for facile solar cell device manufacturing. Instability under ambient conditions occurs, in part, because the organic halide, AX, dissociates into two water-soluble, low-boiling-point species. For example, when $A^+ = CH_3NH_3^+$ and X^- is a halide, AX dissociates into CH_3NH_2 and HX.[11] Exposure to light and dry air has also been reported to decompose $APbX_3$ materials, especially when incorporated in mesostructured assemblies.[12]

One way to improve the stability of $APbX_3$ materials is to increase the size of the organic A^+ moiety and therefore decrease the vapor pressure of its deprotonated form. This design strategy is difficult to implement in $APbX_3$ materials, because they consist of three-dimensional (3D) Pb−X networks of corner-sharing octahedral where the ionic radii of Pb^{2+} and X^- dictate the volume of the cuboctahedral voids, thus limiting the allowable size of the organic group to no larger than the isopropylammonium cation.[13] Alternatively, one-dimensional (1D) and two-dimensional (2D) hybrid organic−inorganic materials offer flexibility to accommodate larger organic groups.[14−18] However, poor orbital overlap between inorganic networks on adjacent 1D chains or 2D sheets precludes efficient electronic conduction that in turn can affect overall solar-cell performance.[19] One strategy to overcome this limitation is to incorporate divalent organic groups in the unit cell to serve as bridges between the inorganic chains or sheets. Such an arrangement may afford more effective conduction if the organic groups have low-lying orbitals to facilitate electronic mixing between the inorganic units and/or may attenuate decomposition due to strong intermolecular interactions afforded by the bridging organic groups. We recently used this strategy to fabricate solar cells that contained a 1D bismuth iodide hybrid organic−inorganic material with bridging hexane-1,6-diammonium divalent organic groups ($HDABiI_5$) as the photoactive layer.[20]

Like 3D $APbX_3$ materials, which were first reported in 1893 and only in the past decade were used as the photoactive layer

Received: December 19, 2018
Accepted: February 6, 2019
Published: February 6, 2019

DOI: 10.1021/acsaem.8b02134
ACS Appl. Energy Mater. 2019, 2, 2178−2187

in solar cells,[21,22] 1D and 2D halide-containing hybrid organic−inorganic materials are not new. In terms of 1D materials, Mousdis et al. reported in 1998 the single-crystal structure of $HDABiI_5$, which they described as a 1D semiconductor.[23] This class of bismuth halide hybrid organic−inorganic materials was further investigated by Mitzi and Brock in the early 2000s,[24] and more recently bismuth halide hybrid organic−inorganic materials have re-emerged as candidates for the photoactive layer in solar cells.[20,25−32] These materials have conductivities in the range of 10^{-9}−10^{-2} S cm^{-1},[25,28] tunable bandgaps in the visible spectral range, high crystal quality, and superior heat and moisture stability compared to state-of-the-art 3D $APbX_3$ materials.[20]

Although 1D hybrid organic−inorganic materials can accommodate larger organic cations in their crystal lattice, which can facilitate control over materials stability, conduction through the inorganic network is limited. This can in part be overcome through use of 2D hybrid organic−inorganic materials, which should still offer flexibility in the allowable size of the organic group as well as superior in-plane conductivity compared to 1D hybrid organic−inorganic materials. The first crystallographic structural data of 2D copper halide hybrid organic−inorganic materials incorporating divalent organic groups were reported in 1988 by Willett et al.[33] These copper halide materials containing $[NH_3(CH_2)_nNH13]^{2+}$ diammonium groups consisted of 2D copper halide sheets arranged in an eclipsed conformation, and materials with n = 3, 4, or 5 were reported to exhibit ferromagnetism.[33] Recently, 2D Ruddlesden−Popper halide perovskite materials have emerged as a promising photoactive layer in solar cells.[17,18] While they are suggested to be more stable than $APbX_3$, to date only those that contain lead or tin have been reported.[34−39]

Copper-based hybrid organic−inorganic halide perovskite materials and related coordination materials are particularly interesting because of the earth abundance and low toxicity of copper.[40−42] Prior work on a quasi-2D copper chloride hybrid organic−inorganic material containing butane-1,4-diammonium was reported by Li and co-workers.[43] In 2016, Cortecchia and co-workers reported a series of photoactive materials that consisted of 2D copper halide sheets with a 2:1 molar ratio of methylammonium monocations (MA^+) to Cu(II).[44] The sunlight-to-electrical power conversion efficiency of a solar cell using $(MA)_2CuBr_2Cl_2$ as the photoactive layer was reported to be 0.017%, with an open-circuit photovoltage of 260 mV.[44] For stability, chloride incorporation in the materials was necessary because the all-bromide-containing $(MA)_2CuBr_4$ was extremely hygroscopic.[44] In a follow-up paper, Cortecchia et al. reported on the incorporation of an organic group within a 2D copper chloride network that contained hydrophobic aromatic units to improve moisture stability.[45] To assess the plausibility of using high-molecular-weight divalent organic groups in 2D copper halide hybrid organic−inorganic materials for applications in solar cells, a comparative study of novel dicationic and monocationic copper halide materials was conducted, and the results are reported herein.

EXPERIMENTAL SECTION

$(HDA)_3Cu_xBr_{8-y}Cl_y$ and $(PA)_6Cu_xBr_8$ Solution Preparation (x ranges from 1 to 2; y = 0, 1, or 2; R = PA or DA). All chemicals were used as received. Hexane-1,6-diammonium bromide ($HDABr_2$) and hexane-1,6-diammonium chloride ($HDACl_2$) were synthesized by slow addition of aqueous hydrobromic acid (HBr, 48% in water, Oakwood Chemical) and aqueous hydrochloric acid (HCl, 37% in water, Macron Fine Chemicals), respectively, at room temperature to a solution of hexane-1,6-diamine (98%, Alfa Aesar) dissolved in methanol (at a 2:1 mole ratio of HBr/HCl to hexane-1,6-diamine) at 0 °C with stirring, followed by continued stirring for 30 min. In a similar manner, *n*-propylammonium bromide (PABr) and n-decylammonium bromide (DABr) were synthesized by slow addition of HBr to a solution of n-propylamine (98%, Alfa Aesar) or n-decylamine (95%, Sigma−Aldrich), respectively, dissolved in methanol (1:1 mole ratio of HBr to *n*-alkylamine). $HDABr_2$, $HDACl_2$, PABr, and DABr precipitates were recovered by evaporation of solvents at 50 °C under reduced pressure. These precipitates were then dissolved in methanol, recrystallized from diethyl ether, and finally vacuum-dried for 12 h.

Organic−inorganic copper bromide solutions were prepared by mixing powders of the organic bromide precursor ($HDABr_2$, PABr, or DABr) and $CuBr_2$ (99%, Alfa Aesar) at a 1:1 molar ratio, but with the organic bromide precursor in slight excess, in 4:1 v/v *N*,*N*-dimethylformamide to dimethyl sulfoxide (4:1 DMF:DMSO) to make a 1 M solution. For $(HDA)_3Cu_xBr_7Cl$ and $(HDA)_3Cu_xBr_6Cl_2$ solutions, a 7:1 molar ratio and 3:1 molar ratio of $HDABr_2$ to $HDACl_2$ were used, respectively. The solutions were stirred at 70 °C inside a nitrogen-filled glovebox, stored in the glovebox until use, and used within 2 weeks of preparation.

For growth of $(HDA)_3Cu_xBr_8$ single crystals, ∼200 μL of a 1 M solution of $(HDA)_3Cu_xBr_8$ in 4:1 v/v DMF:DMSO was dispensed into a 4 mL vial, and this vial was placed uncapped in a 20 mL vial containing ∼2 mL of dichloromethane, which was then capped. $(HDA)_3CuBr_8$ and $(HDA)_3Cu_2Br_8$ single crystals grew overnight in the 4 mL vial via diffusion of dichloromethane.

Materials Processing. All steps of materials deposition and solar cell fabrication were performed in air with 40−60% relative humidity as described below, unless noted otherwise. All thermal treatments were performed using a hot plate. Fluorine-doped tin−oxide-coated glass (FTO) substrates were cleaned as follows: (1) sonicated in Alconox solution, (2) rinsed with deionized water, (3) rinsed with ethanol, (4) sonicated in ethanol, and (5) dried with nitrogen. To deposit the compact TiO_2 ($cTiO_2$) layer, a solution of titanium diisopropoxide bis(acetylacetonate) was pipetted onto a cleaned FTO substrate, and after a 30 s wait period the substrate was spun at 2000 rpm (2000 rpm/s acceleration) for 60 s. The substrate was subsequently dried at 125 °C and then sintered at 550 °C for 30 min. Nanoparticles of TiO_2 were synthesized following a procedure by Ito et al.[46] The nanoparticle solution was further diluted in ethanol at a weight ratio of 1:1 TiO_2 nanoparticle solution:ethanol to make a mesoporous TiO_2 ($mTiO_2$) suspension. The $mTiO_2$ layer was pipetted on top of the $cTiO_2$/FTO substrate, and after a 30 s wait period the substrate was spun at 500 rpm (500 rpm/s acceleration) for 5 s and then 5000 rpm (5000 rpm/s acceleration) for 25 s, dried at 125 °C, and then sintered at 550 °C for 30 min. A conventional method was used to deposit the copper−halide-containing solutions, which was adapted from Kim et al.[47] A filtered copper−halide-containing solution in 4:1 v/v DMF:DMSO was pipetted on top of the $mTiO_2$/$cTiO_2$/FTO substrate, and after a 60 s wait period the substrate was spun at 2000 rpm (2000 rpm/s acceleration) for 60 s, followed by transfer to a hot plate that was preheated to 100 °C and subsequent annealing at 100 °C for 45 min.

Solar Cell Fabrication. Prior to the FTO cleaning step, a region of the FTO film was etched using 2 M aqueous HCl and Zn powder to prevent solar cell shunting upon contact to the top Au electrode. After performing the cleaning steps listed above (Materials Processing subsection), FTO substrates were further cleaned using an O_2 plasma treatment for 10 min. Following deposition of the copper−halide-containing solution per the protocol described above (Materials Processing subsection), a 50 mM solution of 2,2′,7,7′-tetrakis(*N*,*N*′-di-*p*-methoxyphenylamine)-9,9′-spirobifluorene (spiro-OMeTAD) dissolved in toluene was deposited by spin-coating at 3000 rpm (3000 rpm/s acceleration) for 60 s. The solar cells were left to dry in air for 20 min and then were transferred into a nitrogen-filled

DOI: 10.1021/acsaem.8b02134
ACS Appl. Energy Mater. 2019, 2, 2178−2187

glovebox, and 80 nm of Au was thermally evaporated onto the solar cells at a base pressure of 5×10^{-6} mbar. The complete solar cells had an architecture of Au/spiro-OMeTAD/Cu/$mTiO_2$/$cTiO_2$/FTO, where Cu = $(HDA)_3Cu_xBr_8$, $(HDA)_3Cu_xBr_7Cl$, $(HDA)_3Cu_xBr_6Cl_2$, or $(PA)_6Cu_xBr_8$.

Stability Tests. Stability tests were performed in air for $(HDA)_3Cu_xBr_8$ and $(PA)_6Cu_xBr_8$ thin films deposited on $mTiO_2$/$cTiO_2$/FTO per the protocols above (Materials Processing and Solar Cell Fabrication subsections). For the accelerated thermal stability tests, thin films were heated to 100 °C and exposed to ∼50% relative humidity for 16 h. For the moisture stability tests, thin films and powders of $(HDA)_3Cu_xBr_8$ and $(PA)_6Cu_xBr_8$ were exposed to ∼50% relative humidity. The thin films were monitored over a period of 12 days using transmission-mode ultraviolet−visible electronic absorption spectroscopy. The powders were monitored over a period of 14 days using X-ray diffraction.

Materials Characterization. Electronic absorption spectroscopy measurements were performed using an Agilent Cary 60 spectrophotometer with a resolution of 1 nm, and Tauc plots were constructed from the measured spectra. Spectra were corrected for scattering by subtracting a constant value from all data based on the long-wavelength signal, and bandgap energies were determined from best-fit lines of the data near the absorption onset. Electron paramagnetic resonance spectra were collected at 77 K using a Bruker EMX X-band spectrometer. Perpendicular mode spectra represent an average of four scans and were recorded with a microwave frequency of 100 kHz, a modulation amplitude of 10 G, a microwave power of 2 mW, attenuation of 20 dB, a time constant of 82 ms, and a conversion time of 41 ms. Scanning electron microscopy and energy-dispersive X-ray spectroscopy images were acquired on a FEI Magellan 400L XHR. Absorption coefficients of thin films were calculated based on the average thickness measured from cross-sectional scanning electron microscopy images (740 ± 80 nm). For thin films, grazing-incidence X-ray diffraction data were collected using a Rigaku Smartlab diffractometer with Cu Kα radiation and in parallel-beam geometry. For powders, X-ray diffraction data were collected in Bragg−Brentano geometry. Thermogravimetric analysis data were obtained using a TGA Q500 by TA Instruments. Steady-state photoluminescence spectra were acquired at room temperature using a Cary Eclipse fluorescence spectrophotometer by Agilent Technologies with excitation light at 320−350 nm, matched slit widths of 10 nm, and detection in a right-angle geometry. Films were positioned at ∼60° relative to the detector (i.e., ∼30° relative to the incident excitation light). Data were corrected for the wavelength-dependent response of the detection system. Scanning electron microscopy, X-ray diffraction, and X-ray photoelectron spectroscopy measurements were performed at the UC Irvine Materials Research Institute (IMRI).

X-ray photoelectron spectroscopy measurements were performed using a Kratos AXIS Supra photoelectron spectrometer using Al Kα radiation. Cu 2p region scans were obtained immediately following sample z-alignment to minimize X-ray-induced reduction of Cu(II).[48] The X-ray photoelectron spectroscopy data were analyzed using CasaXPS Processing Software. Peaks were fit to Gaussian−Lorentzian (80:20) curves. For X-ray photoelectron spectroscopy measurements of the cutoff region (determination of the work function) and valence-band region (determination of the valence-band maximum), Fermi edge calibration was performed with a sputter-cleaned Ag standard to ensure that all energies were referenced to a common Fermi level (0 eV). X-ray photoelectron spectroscopy measurements were performed instead of ultraviolet photoelectron spectroscopy (UPS) measurements because ultraviolet light has been shown to induce significant work-function reduction on transparent conductive oxide substrate surfaces.[49] Work functions were calculated by extrapolating the X-ray photoelectron spectroscopy cutoff region spectra to the x-intercept. In a manner similar to that performed by Schulz et al.,[50] the low-energy tail of the valence-band spectrum was used to determine the position of the valence-band maximum relative to the Fermi level. By use of the optical bandgaps determined in Figure S1a, the conduction-band minimum was calculated for each copper halide hybrid organic−inorganic material. The conduction-band minimum of TiO_2 and the valence-band maximum of spiro-OMeTAD were taken from a report by Chilvery et al.[51] The Fermi levels with respect to the conduction-band minima and valence-band maxima suggest that the materials are p-type.

Electrical Characterization. An ELH-type W−halogen lamp was used inside a nitrogen-filled glovebox as a source of simulated solar illumination. Before measurement of solar cell current density versus potential (J−E) behavior and chronoamperometry behavior, the light intensity was measured to be ∼1 sun using a calibrated Si photodiode (ThorLabs, Inc., FDS100) positioned at the location of the solar cell. Two-electrode J−E measurements at a scan rate of 100 mV s^{-1} and chronoamperometry measurements were performed using a Gamry Reference 600 potentiostat.

Two-electrode impedance spectroscopy data for a complete solar cell consisting of Au/spiro-OMeTAD/$(HDA)_3Cu_xBr_7Cl$/TiO_2/FTO were collected at reverse-bias DC potentials from 0 to −500 mV in 50 mV increments, and with AC bias amplitudes of ± 10 mV and over frequencies ranging from 2 MHz to 1 Hz. Frequency-dependent data at each DC bias were fit to the standard Randles circuit model, where C_1 is the interfacial capacitance, R_1 is the charge-transfer resistance, and R_2 is the series resistance.[52] The flat-band potential (E_{FB}) and dopant density (N_A) were obtained by best fits of the C_1 versus E data to the following formula:[53]

$$C_1 = \sqrt{\frac{1}{\frac{2}{e\varepsilon_r\varepsilon_0 N_A}\left(E - E_{FB} - \frac{k_B T}{e}\right)}} \quad (1)$$

where e is the elementary charge of an electron (1.6×10^{-19} C), ε_r is the real part of the relative static permittivity (70, value reported by Lin et al. for methylammonium lead triiodide[54]), ε_0 is the permittivity of vacuum (8.854×10^{-14} F cm^{-1}), k_B is the Boltzmann constant (1.38×10^{-23} J K^{-1}), and T is the temperature (298.15 K). These data were plotted as the corresponding Mott−Schottky plot (C_1^{-2} vs E) where the flat-band potential was calculated as (k_BT/e) less than the x-intercept ((6.22 ± 0.03) $\times 10^{15}$ cm^4 F^{-2}). The dopant density (N_A, cm^{-3}) was calculated using the following formula:[55]

$$N_A = \frac{2}{e\varepsilon_r\varepsilon_0 m} \quad (2)$$

where m is the slope of the Mott−Schottky plot ((3.6 ± 0.1) $\times 10^{15}$ cm^4 F^{-2} V^{-1}).

RESULTS AND DISCUSSION

Replacement of organic monocations with half as many organic dications in the syntheses of 2D copper halide hybrid organic−inorganic materials resulted in the formation of new $(HDA)_3Cu_xX_8$ materials, where HDA is hexane-1,6-diammonium (HDA^{2+}) and x = 1 or 2. Single crystals of $(HDA)_3CuBr_8$, in the form of black platelets, were grown from methanol, and the single-crystal structure of $(HDA)_3CuBr_8$ was solved. The unit cell structure is shown in Figure 1. $(HDA)_3CuBr_8$ is monoclinic (space group 14: $P2_1/c$), with lattice constants a = 11.53 Å, b = 17.67 Å, and c = 9.65 Å and unit cell angles α = 90.0°, β = 96.37°, and γ = 90.0°. $CuBr_6$ octahedra are isolated from each other and arrange in quasi-2D sheets along the ab-plane. Single crystals of $(HDA)_3Cu_2Br_8$, in the form of pink needles, also grew in the crystal-growth solution, and the unit cell structure of this material is shown in Figure S2. The formula unit indicates that the oxidation state of copper is 1+, and therefore reduction of the original Cu(II) took place, probably through Br^- oxidation. $(HDA)_3Cu_2Br_8$ is also monoclinic and belongs to space group 14 ($P2_1/c$). In addition, the lattice constants (a = 11.47 Å, b = 16.90 Å, and c = 10.18 Å) and unit cell angles (α = 90.0°, β = 95.21°, and γ = 90.0°) of $(HDA)_3Cu_2Br_8$ are approximately the same as those of $(HDA)_3CuBr_8$, which also results in very

DOI: 10.1021/acsaem.8b02134
ACS Appl. Energy Mater. 2019, 2, 2178−2187

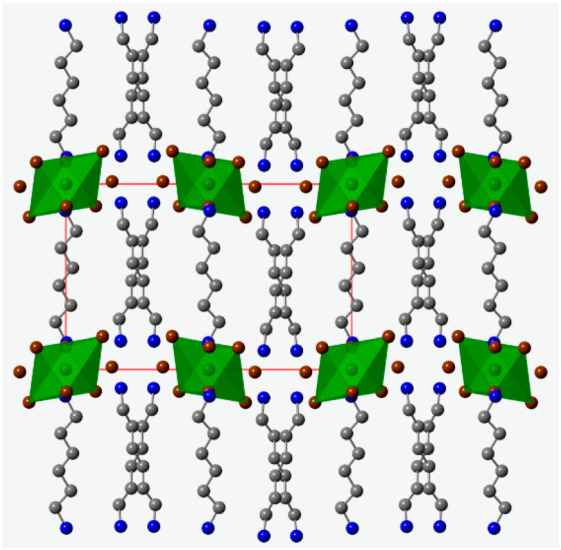

Figure 1. Single-crystal X-ray structure of $(HDA)_3CuBr_8$ as seen from the *b*-axis showing Cu−Br octahedral (green), Cu (green), Br (brown), N (blue), and C (gray). Hydrogen atoms are omitted for clarity.

similar predicted powder X-ray diffraction patterns for the two materials. Concurrent with the growth of $(HDA)_3Cu_2Br_8$ single crystals, single crystals of $(HDA)_3CuBr_8$ lost their single-crystal structural integrity and became powders. Electron paramagnetic resonance spectra of the crystal growth solution were obtained 1 week after the initiation of single-crystal growth and spectra confirmed that some of the original Cu(II) in the solution remained in the 2+ state (Figure S3).

Transmission-mode ultraviolet−visible electronic absorption spectra for air-processed solution-cast thin films of $(HDA)_3Cu_xBr_8$ and an analogous material incorporating twice as many *n*-propylammonium (PA^+) groups per copper atom, $(PA)_6Cu_xBr_8$, are shown in Figure 2a. These materials exhibit absorption features that are similar to those of MA_2CuX_4 materials.[44] PA^+ was chosen for comparative studies because its C−N core is roughly half the length of the C−N core of HDA^{2+}. Accompanying Tauc plots and digital photograph images for a series of freshly prepared $(HDA)_3Cu_xBr_{8-y}Cl_y$ thin films, where y = 0, 1, or 2, are shown as Figures S1 and S4, respectively. Each thin film exhibited a lowest energy indirect bandgap of ∼1.80 eV (Figure S1a), a direct bandgap of ∼2.05−2.10 eV (Figure S1b), and d−d transitions at ∼1.60 eV (Figure S1a). These data suggest that the bandgaps of the materials are not greatly affected by the replacement of up to 25% of the bromides with chlorides. The indirect bandgap of these materials is ∼0.25 eV smaller than that of thin films of $HDABiI_5$,[20] making them more suitable for applications as the photoactive layer in the top cell of a tandem solar cell with silicon.[6,7] Bandgap energies and molar absorption coefficients are comparable to those reported for monocationic copper halide hybrid organic−inorganic materials.[44] Interestingly, the $(PA)_6Cu_xBr_8$ thin film exhibited the weakest molar absorptivity of the series, which suggests that incorporation of divalent organic groups in these materials causes enhancement of their absorption cross sections.

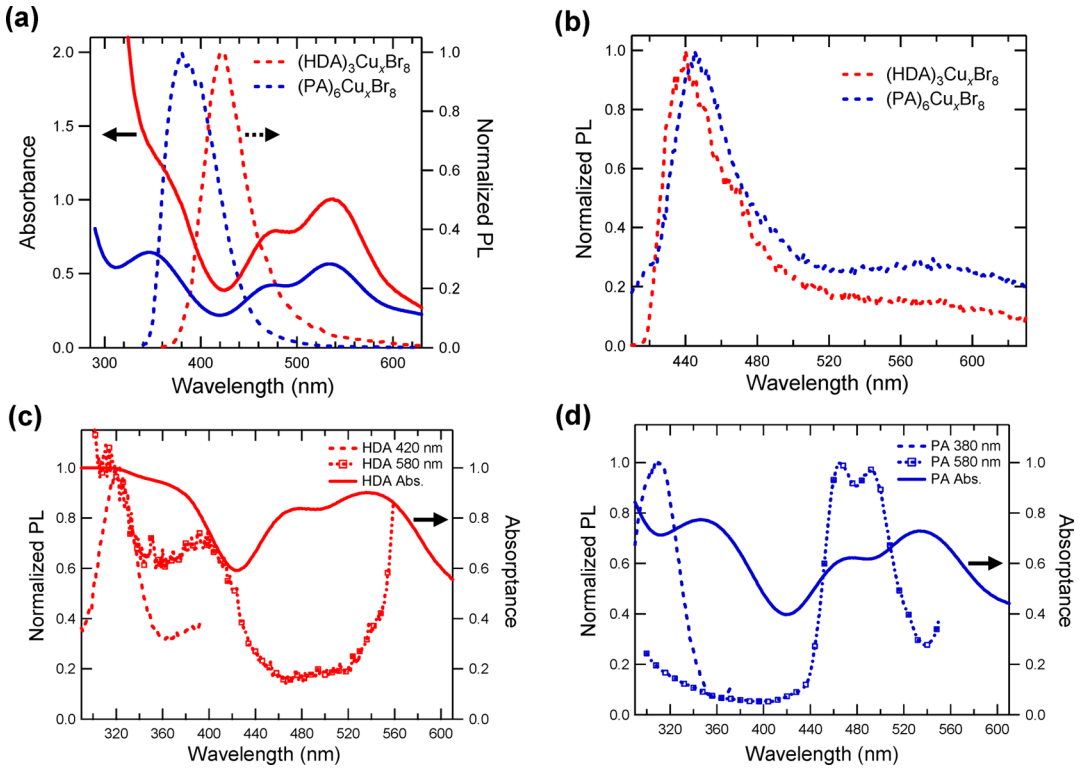

Figure 2. (a) Transmission-mode electronic absorption spectra (dashed lines) and steady-state photoluminescence (PL) emission spectra (solid lines, $\lambda_{ex} \approx 340$ nm) of thin films of $(HDA)_3Cu_xBr_8$ and $(PA)_6Cu_xBr_8$. (b) Normalized steady-state PL emission spectra ($\lambda_{ex} \approx 400$ nm) of thin films of $(HDA)_3Cu_xBr_8$ and $(PA)_6Cu_xBr_8$, showing a broad tailing region with $\lambda_{max} \approx 580$ nm. Absorptance spectra (solid lines) and steady-state PL excitation spectra of (c) $(HDA)_3Cu_xBr_8$ and (d) $(PA)_6Cu_xBr_8$ probed at PL peak wavelengths of 420 nm and 380 nm, respectively, (dashed lines) and at 580 nm (squares with dotted lines).

DOI: 10.1021/acsaem.8b02134
ACS Appl. Energy Mater. 2019, 2, 2178−2187

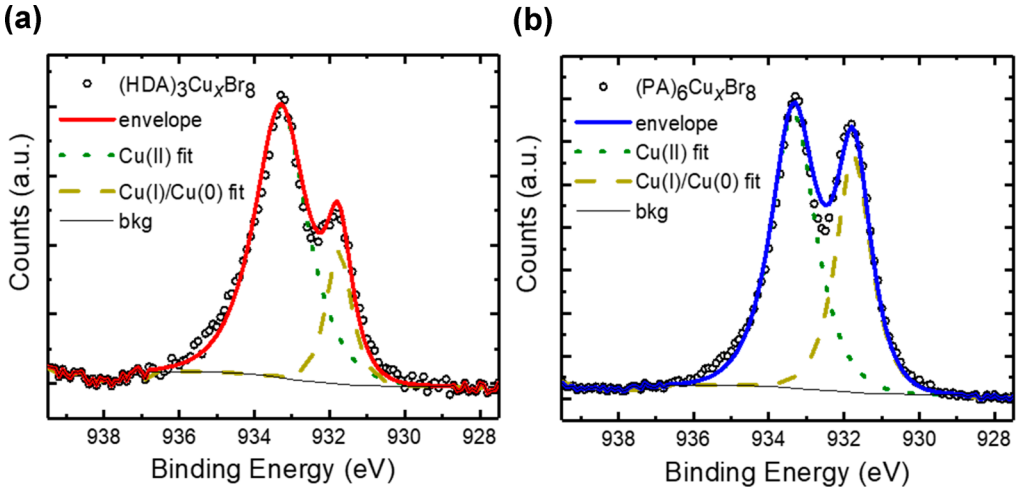

Figure 3. X-ray photoelectron spectra of the Cu $2p_{3/2}$ region of thin films of (a) $(HDA)_3Cu_xBr_8$ and (b) $(PA)_6Cu_xBr_8$ on fluorine-doped tin−oxide-coated glass substrates. Best fits to the Cu $2p_{3/2}$ peaks are shown, where envelope is the sum of the Cu(II) fit, the Cu(I)/Cu(0) fit, and a Shirley background (bkg).

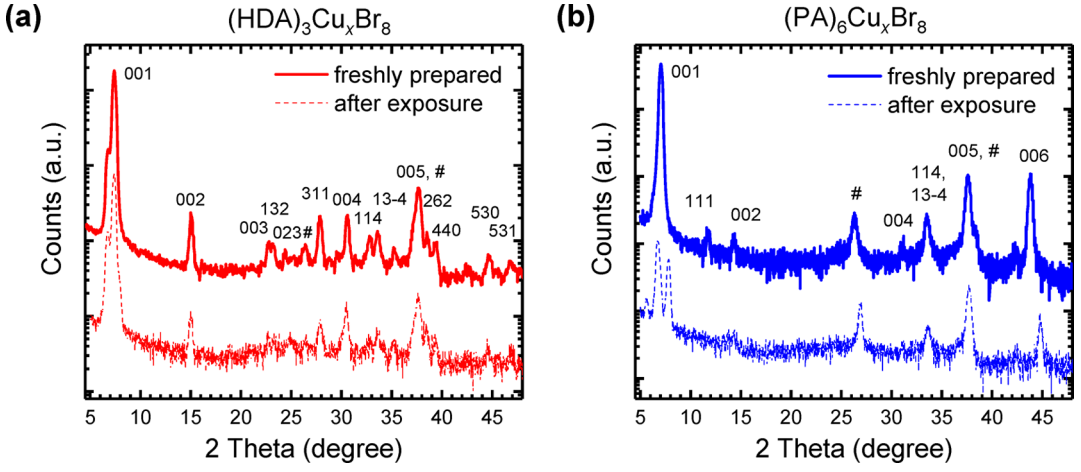

Figure 4. Grazing-incidence X-ray diffraction patterns of thin films of (a) $(HDA)_3Cu_xBr_8$ and (b) $(PA)_6Cu_xBr_8$ when freshly prepared and after exposure to 100 °C and ∼50% relative humidity for 16 h. # denotes peaks associated with the underlying fluorine-doped tin−oxide-coated glass substrate.

Steady-state photoluminescence at room temperature was observed from thin films of $(HDA)_3Cu_xBr_8$ and $(PA)_6Cu_xBr_8$ (Figure 2a), which is indicative of high materials quality.[56] The emission peaks exhibited much smaller Stokes shifts (0.49 eV in $(HDA)_3Cu_xBr_8$ and 0.31 eV in $(PA)_6Cu_xBr_8$) than in previously reported MA_2CuX_4 materials (1.3 eV), which suggests less electronic and nuclear reorganization in the excited states of the copper bromide materials reported herein.[44] When the excitation wavelength was adjusted from 340 to 400 nm, a new broad, weak emission band was apparent at ∼580 nm (Figure 2b) that has not been reported previously for copper halide hybrid organic−inorganic materials. The weakness of this emission band suggests that its emission quantum yield is poor or that the electronic transition that gives rise to this emission band has a small absorption cross section at ∼400 nm or is present at a low concentration in the film (Figure 2c,d). Excitation at 400 nm resulted in emission spectra that tailed out to beyond 620 nm, where $(HDA)_3Cu_xBr_8$ still exhibited >10% of its maximum emission signal intensity and $(PA)_6Cu_xBr_8$ still exhibited >20% of its maximum emission signal intensity (Figure 2b). Emission in this wavelength region for analogous MA_2CuX_4 materials has been attributed to recombination via Cu(I) trap states that likely form during film annealing.[44]

The speciation of atoms near the surface of thin films was characterized by X-ray photoelectron spectroscopy. Scans of the Cu 2p core level binding energy range revealed the presence of Cu(II) and other peak(s) due to Cu(I) and/or Cu(0) (Figure 3 and Figure S5), which is consistent with the single-crystal structural data (Figure 1 and Figure S2) and absorptance and photoluminescence spectra (Figure 2). Deciphering between characteristic peaks corresponding to Cu(I) and Cu(0) is a challenge because Cu(I) and Cu(0) exhibit very similar binding energies. Peak fitting of the Cu $2p_{3/2}$ peaks revealed the copper composition profile of $(HDA)_3Cu_xBr_8$ to be approximately 81% Cu(II) and 19% Cu(I)/Cu(0) (Figure 3a) and for $(PA)_6Cu_xBr_8$, approximately 66% Cu(II) and 34% Cu(I)/Cu(0) (Figure 3b). These data suggest that reductive degradation of the inorganic precursor material, $CuBr_2$, occurred during thin-film fabrication, which resulted in the formation of $(HDA)_3Cu_2Br_8$ (Figure S2). Scans of the Cl 2p region revealed near-surface speciation of chlorine species in the $(HDA)_3Cu_xBr_5Cl_3$ and $(HDA)_3Cu_xBr_6Cl_2$ samples and no observed chlorine species in the

DOI: 10.1021/acsaem.8b02134
ACS Appl. Energy Mater. 2019, 2, 2178−2187

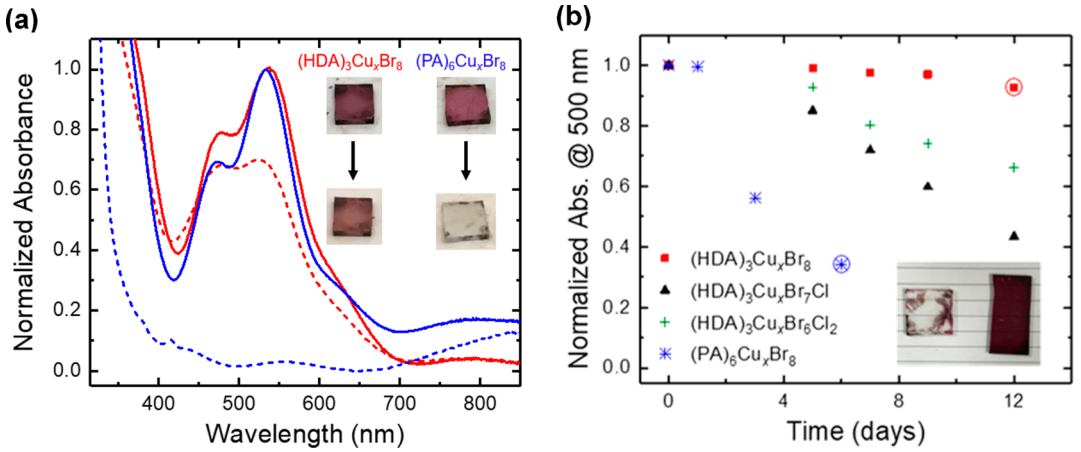

Figure 5. (a) Transmission-mode absorption spectra of thin films of $(HDA)_3Cu_xBr_8$ (red) and $(PA)_6Cu_xBr_8$ (blue) freshly prepared (solid lines) and after exposure to 100 °C and ∼50% relative humidity for 16 h (dashed lines), each corrected for background scattering. Inset: digital photograph images of the thin films before (top) and after (bottom) exposure. (b) Normalized absorbance at 500 nm as a function of time for the copper halide hybrid organic−inorganic thin films at room temperature and 50% relative humidity. Inset: digital photograph image of $(PA)_6Cu_xBr_8$ after 6 days (left; blue circle in main figure) and $(HDA)_3Cu_xBr_8$ after 12 days (right; red circle in main figure).

$(HDA)_3Cu_xBr_8$ and $(PA)_6Cu_xBr_8$ samples (Figure S6). Following continued X-ray exposure, through measurements of survey spectra and other core level binding energy regions, the $(HDA)_3Cu_xBr_8$ thin film contained approximately 75% Cu(II) and 25% Cu(I)/Cu(0) (Figure S5a) and the $(PA)_6Cu_xBr_8$ thin film contained approximately 60% Cu(II) and 40% Cu(I)/Cu(0) (Figure S5b), which marked a ∼6% increase in near-surface Cu(I)/Cu(0) for both thin films. The small magnitude of these X-ray-induced changes provide evidence that there is Cu(I)/Cu(0) present in both thin films before exposure to the X-ray beam. The larger percentage of reduced copper species in thin films of $(PA)_6Cu_xBr_8$ supports observations of faster degradation of the Cu(II)-containing $(PA)_6Cu_xBr_8$ thin films in comparison to the Cu(II)-containing $(HDA)_3Cu_xBr_8$ thin films. Scans of the C 1s, N 1s, and Br 3p core level binding energy ranges for thin films of $(HDA)_3Cu_xBr_8$ and $(PA)_6Cu_xBr_8$ were also performed (Figure S7). For both samples, the C 1s region spectra reveal the presence of two peaks, which correspond to C−C bonds and C−N bonds in the organic groups. The N 1s region spectra contain a peak at 401.2 eV, which is consistent with the N 1s peak position for $MAPbX_3$ materials and is attributed to the nitrogen atoms in the ammonium groups.[57] Strong Br 3p peaks were observed in $(HDA)_3Cu_xBr_8$ and $(PA)_6Cu_xBr_8$ thin films due to their large bromide content.

Evaluation of crystallinity and thermal stability was performed using grazing-incidence X-ray diffraction. X-ray diffraction patterns of freshly prepared annealed thin films of dicationic $(HDA)_3Cu_xBr_8$ (Figure 4a, solid red line) and analogous monocationic $(PA)_6Cu_xBr_8$ (Figure 4b, solid blue line) show strong preferential orientation in the [001] direction, which is similar to the patterns reported by Cortecchia et al.[44] This indicates that the quasi-2D copper halide sheets are oriented in-plane with the fluorine-doped tin−oxide-coated glass substrate. The observation of larger higher-order peaks in the $(HDA)_3Cu_xBr_8$ pattern in comparison to the $(PA)_6Cu_xBr_8$ pattern indicates that there is greater extent of ordering at each Bragg reflection condition in the $(HDA)_3Cu_xBr_8$ thin film.[44] Because the *c*-axis is orthogonal to the quasi-2D copper halide sheets, the value of *c* is the sheet spacing and can be determined from the 2θ values. For $(HDA)_3Cu_xBr_8$, the (001) peak occurs at 2θ = 7.80°, which indicates a sheet spacing of 11.3 Å. This value is consistent with the sheet spacing determined from single-crystal X-ray diffraction, which was 11.2 Å. In comparison, the sheet spacing for $(PA)_6Cu_xBr_8$ is 12.6 Å, which was calculated from a $(PA)_6Cu_xBr_8$ (001) 2θ value of 7.04°. The difference between sheet spacing in $(HDA)_3Cu_xBr_8$ and $(PA)_6Cu_xBr_8$ is logical based on the slightly larger size of two PA^+ in comparison to one HDA^{2+}. A comparison of powder versus thin-film X-ray diffraction patterns for both $(HDA)_3Cu_xBr_8$ and $(PA)_6Cu_xBr_8$ is shown in Figure S8. Unlike for $(HDA)_3Cu_xBr_8$, the largest-intensity peak for the $(PA)_6Cu_xBr_8$ powder occurred at a larger 2θ value relative to that of the thin film, which is speculated to be due to water molecules present in $(PA)_6Cu_xBr_8$ powder, which would suggest $(PA)_6Cu_xBr_8$ is more hygroscopic than $(HDA)_3Cu_xBr_8$ since they were processed in nominally identical manners.

Accelerated thermal stability tests on thin films of $(HDA)_3Cu_xBr_8$ resulted in minimal changes in the grazing-incidence X-ray diffraction pattern (Figure 4a) and absorption spectrum (Figure 5a, red data) in comparison to changes observed for thin films of $(PA)_6Cu_xBr_8$ after the same treatment (Figures 4b and 5a, blue data). For $(PA)_6Cu_xBr_8$ thin films, the (001) peak intensity decreased significantly, the (001) peak shifted to 6.70°, and new peaks emerged at 2θ values of 5.66° and 7.80°. Accelerated thermal stability tests using thermogravimetric analysis under an inert atmosphere on powders originating from thin films showed similar trends when performed on $(HDA)_3Cu_xBr_8$ and $(PA)_6Cu_xBr_8$ (Figure S9) and when performed directly on bromide salts of the dicationic and monocationic organic moieties, i.e., $HDABr_2$ and PABr precursor powders (Figure S10). The same thermogravimetric analyses were performed on the material $(DA)_6Cu_xBr_8$, where DA^+ is the 1-decylammonium monocation ($C_{10}H_{21}$-NH_3^+), and the DABr precursor powder. Protonated decylamine was chosen for comparative thermal stability tests because of the similar boiling point of decylamine (217 °C) to hexane-1,6-diamine (204 °C). The results show that copper bromide materials as well as precursor powders containing HDA^+ can withstand the greatest amount of thermal input (Figures S9 and S10), indicating that

DOI: 10.1021/acsaem.8b02134
ACS Appl. Energy Mater. 2019, 2, 2178−2187

deprotonation and halide coordination are a contributing deterrent to thermal gasification. These data suggest that for hybrid organic−inorganic materials that can accommodate organic moieties with a net charge of 2+ per formula unit, the presence of divalent organic groups in the unit cell of thermally annealed thin films greatly enhances thermal stability. Cortecchia et al. reported that partial substitution of bromide for chloride in $(MA)_2CuBr_4$ improved crystallinity and moisture tolerance.[44] However, Lichty et al. speculated that chloride-containing phases should be more soluble in water at room temperature than bromide-containing phases, which may accelerate the degradation process of the chloride-containing films.[58] Herein, moisture stability studies on thin films of $(HDA)_3Cu_xBr_{8-y}Cl_y$, where y = 0, 1, or 2, and $(PA)_6Cu_xBr_8$ indicated a trend consistent with aqueous solubility where thin films of $(HDA)_3Cu_xBr_8$ were more tolerant to ambient moisture (Figure 5b and Figure S11).

Solar cells were fabricated from the 2D $(HDA)_3Cu_xBr_{8-y}Cl_y$ materials. All of the material layers were deposited in air except for the gold top contact. A cross-sectional scanning electron microscopy image of a representative solar cell containing $(HDA)_3Cu_xBr_7Cl$ as the light-absorbing layer is shown in Figure 6. This scanning electron microscopy image reveals that the $(HDA)_3Cu_xBr_7Cl$ layer is smooth, continuous, and, on average, roughly 200 nm thick. The mesoporous TiO_2 scaffold is not visible as it is coated by the $(HDA)_3Cu_xBr_7Cl$ layer. Energy-dispersive X-ray spectroscopy mapping data of the $(HDA)_3Cu_xBr_8$ thin-film cross section are shown in Figure S12, which supports the location of elements within the $(HDA)_3Cu_xBr_8$, TiO_2, and fluorine-doped tin oxide-coated glass (FTO) layers.

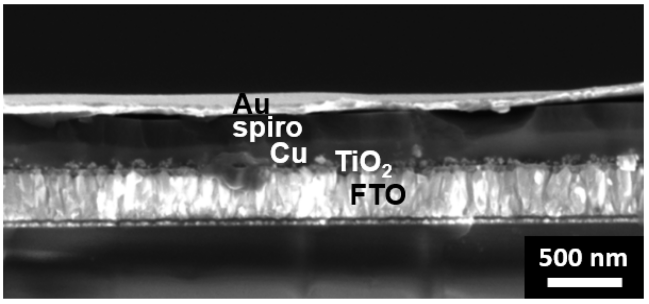

Figure 6. Cross-sectional scanning electron micrograph of a representative solar cell containing $(HDA)_3Cu_xBr_7Cl$ as the photoactive layer and where spiro is spiro-OMeTAD, Cu is $(HDA)_3Cu_xBr_7Cl$, TiO_2 is a compact TiO_2 layer, and FTO is a fluorine-doped tin−oxide-coated glass substrate.

The photovoltaic performances of these materials as solar cells are shown in Figure 7a. Solar cells containing $(HDA)_3Cu_xBr_7Cl$ as the photoactive layer yielded the largest short-circuit photocurrent densities, which may be attributed to the improved crystallinity due to partial substitution of bromide for chloride.[36] The best-performing solar cell, with an active area of 0.25 cm^2, exhibited an open-circuit photovoltage (V_{oc}) of 240 mV, a short-circuit photocurrent density (J_{sc}) of ~30 $\mu A\ cm^{-2}$, and a fill factor of 0.30, resulting in a light-to-electrical power conversion efficiency of ~0.002%. A similar-sized solar cell containing $(HDA)_3Cu_xBr_8$ exhibited a much larger V_{oc} of >400 mV but a smaller J_{sc} of ~10 $\mu A\ cm^{-2}$. Two-electrode impedance spectroscopy was used to determine the flat-band potential and dopant density of $(HDA)_3Cu_xBr_7Cl$. A nonlinear least-squares best fit of the $C-E$ data, depicted in the form of a Mott−Schottky plot (Figure 7b), indicates a flat-band potential of 1.7 ± 0.2 V and a dopant density of ~6 × $10^{17}\ cm^{-3}$, where calculations are provided in the Experimental Section. The maximum valence band energies of $(HDA)_3Cu_xBr_{8-y}Cl_y$ materials were calculated based on low-intensity X-ray photoelectron spectroscopy data reporting on the work function (Figure S13) and the valence band (Figure S14). From these measurements it was determined that the spiro-OMeTAD/$(HDA)_3Cu_xBr_8$ interface and the $(HDA)_3Cu_xBr_8/TiO_2$ interface are responsible for combined losses in photovoltage that exceed 750 mV (Figure S15). Therefore, the electron-transport layer and hole-transport layers of $(HDA)_3Cu_xBr_{8-y}Cl_y$-containing solar cells can be optimized to achieve larger V_{oc} values. The energy difference between the conduction-band minimum and Fermi level in $(HDA)_3Cu_xBr_7Cl$ is 1.2 eV, which is in modest agreement with the flat-band potential calculated from Figure 7b. Additional analysis associated with the X-ray photoelectron spectroscopy data is provided in the Experimental Section.

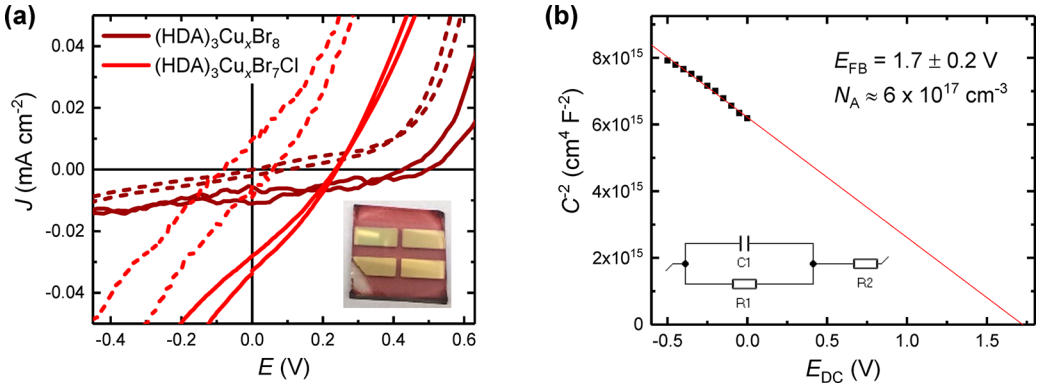

Figure 7. (a) $J-E$ behavior for solar cells consisting of Au/spiro-OMeTAD/Cu/TiO_2/FTO, where Cu stands for $(HDA)_3Cu_xBr_8$ or $(HDA)_3Cu_xBr_7Cl$. Solid lines represent measurements under 1 sun irradiance, and dashed lines represent dark measurements. Inset: digital photograph image of a complete solar cell. (b) Impedance spectroscopy data, presented as a Mott−Schottky plot, for a solar cell consisting of Au/spiro-OMeTAD/$(HDA)_3Cu_xBr_7Cl/TiO_2$/FTO and with the calculated flat-band potential (E_{FB}) and dopant density (N_A). Inset: standard Randles circuit used to model the impedance spectroscopy data.

DOI: 10.1021/acsaem.8b02134
ACS Appl. Energy Mater. 2019, 2, 2178−2187

CONCLUSIONS

With the aim to mitigate materials instability and toxicity and therefore provide greater flexibility during solar cell device manufacturing, new 2D copper halide hybrid organic–inorganic materials incorporating divalent organic groups were synthesized and characterized. Electronic absorption spectra suggest indirect optical bandgaps of ∼1.8 eV, and photoluminescence spectra indicate the presence of emissive Cu(I) trap states. X-ray photoelectron spectroscopy data confirmed surface elemental composition of these materials and supported the faster degradation during sample processing observed for $(PA)_6Cu_xBr_8$ in comparison to $(HDA)_3Cu_xBr_8$, possibly due to reduction of Cu(II) to Cu(I)/Cu(0). Grazing-incidence X-ray diffraction data confirmed crystallinity and indicated preferential orientation in the [001] direction such that the copper halide sheets were oriented in-plane with the substrate. $(HDA)_3Cu_xBr_8$ demonstrated superior stability to heat and moisture in comparison to analogous monocationic copper halide materials containing three-carbon or ten-carbon chains, $(PA)_6Cu_xBr_8$ and $(DA)_6Cu_xBr_8$, respectively. Photophysical measurements on best-performing solar cells containing $(HDA)_3Cu_xBr_8$ demonstrated an open-circuit photovoltage in excess of 400 mV, and a short-circuit photocurrent of ∼30 μA cm^{-2} was obtained when the light absorber was changed to $(HDA)_3Cu_xBr_7Cl$. These values are similar to those reported for analogous state-of-the-art materials containing organic monocations.

ASSOCIATED CONTENT

Supporting Information

The Supporting Information is available free of charge on the ACS Publications website at DOI: 10.1021/acsaem.8b02134.

Tauc plots, single-crystal X-ray structure of $(HDA)_3Cu_2Br_8$, X-band electron paramagnetic resonance spectrum, digital photograph images of thin films, additional X-ray photoelectron spectra, additional X-ray diffraction patterns, temperature-dependent thermogravimetric analysis data, energy-dispersive X-ray spectroscopy mapping data, and energy-level diagrams (PDF)

AUTHOR INFORMATION

Corresponding Author

*E-mail ardo@uci.edu.

ORCID

Shane Ardo: 0000-0001-7162-6826

Notes

The authors declare no competing financial interest.

ACKNOWLEDGMENTS

The authors acknowledge support from the Alfred P. Sloan Foundation under Grant FG-2017-8888, the 2017 UC MEXUS-CONACYT Collaborative Research Grant under Grant UCM-208101, and the School of Physical Sciences at the University of California Irvine (UC Irvine). D.M.F. acknowledges support by the DOE, Office of Science, Office of Workforce Development for Teachers and Scientists, Office of Science Graduate Student Research (SCGSR) program under Contract DE-SC0014664 and by the National Science Foundation Graduate Research Fellowship under Grant DGE-1321846. X-ray photoelectron spectroscopy work was performed at the UC Irvine Materials Research Institute (IMRI) using instrumentation funded in part by the National Science Foundation Major Research Instrumentation Program under Grant CHE-1338173. The authors thank Meghen Goulet for assistance with electron paramagnetic resonance measurements. Photoluminescence experiments were performed at the UC Irvine Laser Spectroscopy Laboratory under the supervision of its director, Dr. Dima Fishman. The authors thank Dr. Ich Tran (UC Irvine) for guidance in X-ray photoelectron spectroscopy data analysis, Dr. Qiyin Lin (UC Irvine) for guidance in X-ray diffraction data analysis, Mikey Wojnar and Austin Ryan for assistance with single-crystal X-ray diffraction data acquisition and analysis, and Brenda Vargas (Universidad Nacional Autónoma de México) for helpful discussions. The authors also thank group members of the laboratory of Prof. Matt Law (UC Irvine) for providing training and access to their O_2 plasma cleaner and thermal evaporator.

REFERENCES

(1) Seok, S. I.; Grätzel, M.; Park, N.-G. Methodologies toward Highly Efficient Perovskite Solar Cells. *Small* **2018**, *14*, 1704177.

(2) Eperon, G. E.; Hörantner, M. T.; Snaith, H. J. Efficient and stable Solution-processed planar perovskite solar cells via contact passivation. *Nat. Rev. Chem.* **2017**, *1*, 0095.

(3) Leijtens, T.; Bush, K.; Cheacharoen, R.; Beal, R.; Bowring, A.; McGehee, M. D. Towards enabling stable lead halide perovskite solar cells; interplay between structural, environmental, and thermal stability. *J. Mater. Chem. A* **2017**, *5*, 11483.

(4) Green, M. A.; Hishikawa, Y.; Dunlop, E. D.; Levi, D. H.; Hohl-Ebinger, J.; Ho-Baillie, A. W. Y. Solar cell efficiency tables (version 51). *Prog. Photovoltaics* **2018**, *26*, 3.

(5) Saliba, M.; Matsui, T.; Seo, J.-Y.; Domanski, K.; Correa-Baena, J.-P.; Nazeeruddin, M. K.; Zakeeruddin, S. M.; Tress, W.; Abate, A.; Hagfeldt, A.; Gratzel, M. Cesium-containing triple cation perovskite solar cells: improved stability, reproducibility and high efficiency. *Energy Environ. Sci.* **2016**, *9*, 1989.

(6) Albrecht, S.; Saliba, M.; Correa Baena, J. P.; Lang, F.; Kegelmann, L.; Mews, M.; Steier, L.; Abate, A.; Rappich, J.; Korte, L.; Schlatmann, R.; Nazeeruddin, M. K.; Hagfeldt, A.; Grätzel, M.; Rech, B. Monolithic perovskite/silicon-heterojunction tandem solar cells processed at low temperature. *Energy Environ. Sci.* **2016**, *9*, 81.

(7) Bush, K. A.; Palmstrom, A. F.; Yu, Z. J.; Boccard, M.; Cheacharoen, R.; Mailoa, J. P.; Mcmeekin, D. P.; Hoye, R. L. Z.; Bailie, C. D.; Leijtens, T.; Peters, I. M.; Minichetti, M. C.; Rolston, N.; Prasanna, R.; Sofia, S.; Harwood, D.; Ma, W.; Moghadam, F.; Snaith, H. J.; Buonassisi, T.; Holman, Z. C.; Bent, S. F.; McGehee, M. D. 23.6%-efficient monolithic perovskite/silicon tandem solar cells with improved stability. *Nat. Energy* **2017**, *2*, 17009.

(8) Saparov, B.; Mitzi, D. B. Organic–Inorganic Perovskites: Structural Versatility for Functional Materials Design. *Chem. Rev.* **2016**, *116*, 4558.

(9) Slavney, A. H.; Smaha, R. W.; Smith, I. C.; Jaffe, A.; Umeyama, D.; Karunadasa, H. I. Chemical Approaches to Addressing the Instability and Toxicity of Lead–Halide Perovskite Absorbers. *Inorg. Chem.* **2017**, *56*, 46.

(10) Leijtens, T.; Eperon, G. E.; Noel, N. K.; Habisreutinger, S. N.; Petrozza, A.; Snaith, H. J. Stability of metal halide perovskite solar cells. *Adv. Energy Mater.* **2015**, *5*, 1500963.

(11) Misra, R. K.; Aharon, S.; Li, B.; Mogilyansky, D.; Visoly-Fisher, I.; Etgar, L.; Katz, E. A. Temperature- and Component-Dependent Degradation of Perovskite Photovoltaic Materials under Concentrated Sunlight. *J. Phys. Chem. Lett.* **2015**, *6*, 326.

(12) Aristidou, N.; Sanchez-Molina, I.; Chotchuangchutchaval, T.; Brown, M.; Martinez, L.; Rath, T.; Haque, S. A. The Role of Oxygen in the Degradation of Methylammonium Lead Trihalide Perovskite Photoactive Layers. *Angew. Chem., Int. Ed.* **2015**, *54*, 8208.

DOI: 10.1021/acsaem.8b02134
ACS Appl. Energy Mater. 2019, 2, 2178–2187

(13) Becker, M.; Klüner, T.; Wark, M. Joint Space-Time Coherent Vibration Driven Conformational Transitions in a Single Molecule. *Dalt. Trans.* **2017**, *46*, 3500.
(14) Liang, K.; Mitzi, D. B.; Prikas, M. T. Synthesis and Characterization of Organic−Inorganic Perovskite Thin Films Prepared Using a Versatile Two-Step Dipping Technique. *Chem. Mater.* **1998**, *10*, 403.
(15) Mitzi, D. B.; Chondroudis, K.; Kagan, C. R. Design, Structure, and Optical Properties of Organic−Inorganic Perovskites Containing an Oligothiophene Chromophore. *Inorg. Chem.* **1999**, *38*, 6246.
(16) Mitzi, D. B. Organic−Inorganic Perovskites Containing Trivalent Metal Halide Layers: The Templating Influence of the Organic Cation Layer. *Inorg. Chem.* **2000**, *39*, 6107.
(17) Smith, I. C.; Hoke, E. T.; Solis-Ibarra, D.; McGehee, M. D.; Karunadasa, H. I. A Layered Hybrid Perovskite Solar-Cell Absorber with Enhanced Moisture Stability. *Angew. Chem., Int. Ed.* **2014**, *53*, 11232.
(18) Cao, D.; Stoumpos, C. C.; Farha, O. K.; Hupp, J. T.; Kanatzidis, M. G. 2D Homologous Perovskites as Light-Absorbing Materials for Solar Cell Applications. *J. Am. Chem. Soc.* **2015**, *137*, 7843.
(19) Misra, R. K.; Cohen, B.-E.; Iagher, L.; Etgar, L. Low-Dimensional Organic−Inorganic Halide Perovskite: Structure, Properties, and Applications. *ChemSusChem* **2017**, *10*, 3712.
(20) Fabian, D. M.; Ardo, S. Hybrid organic−inorganic solar cells based on bismuth iodide and 1,6-hexanediammonium dication. *J. Mater. Chem. A* **2016**, *4*, 6837.
(21) Wells, H. L. Über die Cäsium- und Kalium-Bleihalogenide. *Z. Anorg. Chem.* **1893**, *3*, 195.
(22) Kojima, A.; Teshima, K.; Shirai, Y.; Miyasaka, T. Organometal Halide Perovskites as Visible-Light Sensitizers for Photovoltaic Cells. *J. Am. Chem. Soc.* **2009**, *131*, 6050.
(23) Mousdis, G. A.; Papavassiliou, G. C.; Terzis, A.; Raptopoulou, C. P. Preparation, Structures and Optical Properties of $[H_3N(CH_2)_6NH_3]BiX_5$ (X = I, Cl) and $[H_3N(CH_2)_6NH_3]SbX_5$ (X = I, Br). *Z. Z. Naturforsch., B: J. Chem. Sci.* **1998**, *53b*, 927.
(24) Mitzi, D. B.; Brock, P. Structure and Optical Properties of Several Organic−Inorganic Hybrids Containing Corner-Sharing Chains of Bismuth Iodide Octahedra. *Inorg. Chem.* **2001**, *40*, 2096.
(25) Brandt, R. E.; Kurchin, R. C.; Hoye, R. L. Z.; Poindexter, J. R.; Wilson, M. W. B.; Sulekar, S.; Lenahan, F.; Yen, P. X. T.; Stevanović, V.; Nino, J. C.; Bawendi, M. G.; Buonassisi, T. Investigation of Bismuth Triiodide (BiI_3) for Photovoltaic Applications. *J. Phys. Chem. Lett.* **2015**, *6*, 4297.
(26) Lehner, A. J.; Fabini, D. H.; Evans, H. A.; Hébert, C.-A.; Smock, S. R.; Hu, J.; Wang, H.; Zwanziger, J. W.; Chabinyc, M. L.; Seshadri, R. Crystal and Electronic Structures of Complex Bismuth Iodides $A_3Bi_2I_9$ (A = K, Rb, Cs) Related to Perovskite: Aiding the Rational Design of Photovoltaics. *Chem. Mater.* **2015**, *27*, 7137.
(27) Park, B. W.; Philippe, B.; Zhang, X.; Rensmo, H.; Boschloo, G.; Johansson, E. M. J. Bismuth Based Hybrid Perovskites $A_3Bi_2I_9$ (A: Methylammonium or Cesium) for Solar Cell Application. *Adv. Mater.* **2015**, *27*, 6806.
(28) Lyu, M.; Yun, J. H.; Cai, M.; Jiao, Y.; Bernhardt, P. V.; Zhang, M.; Wang, Q.; Du, A.; Wang, H.; Liu, G.; Wang, L. Organic−inorganic bismuth (III)-based material: A lead-free, air-stable and solution-processable light-absorber beyond organolead perovskites. *Nano Res.* **2016**, *9*, 692.
(29) Hoye, R.; Brandt, R. E.; Osherov, A.; Stevanovic, V.; Stranks, S. D.; Wilson, M. W. B.; Kim, H.; Akey, A. J.; Kurchin, R. C.; Poindexter, J. R.; Wang, E. N.; Bawendi, M. G.; Bulovic, V.; Buonassisi, T. Methylammonium bismuth iodide as a lead-free, stable hybrid organic-inorganic solar absorber. *Chem. - Eur. J.* **2016**, *22*, 2605.
(30) Slavney, A. H.; Hu, T.; Lindenberg, A. M.; Karunadasa, H. I. A Bismuth-Halide Double Perovskite with Long Carrier Recombination Lifetime for Photovoltaic Applications. *J. Am. Chem. Soc.* **2016**, *138*, 2138.
(31) Volonakis, G.; Filip, M. R.; Haghighirad, A. A.; Sakai, N.; Wenger, B.; Snaith, H. J.; Giustino, F. Lead-Free Halide Double Perovskites via Heterovalent Substitution of Noble Metals. *J. Phys. Chem. Lett.* **2016**, *7*, 1254.
(32) Bass, K. K.; Estergreen, L.; Savory, C. N.; Buckeridge, J.; Scanlon, D. O.; Djurovich, P. I.; Bradforth, S. E.; Thompson, M. E.; Melot, B. C. Vibronic Structure in Room Temperature Photoluminescence of the Halide Perovskite $Cs_3Bi_2Br_9$. *Inorg. Chem.* **2017**, *56*, 42.
(33) Willett, R.; Place, H.; Middleton, M. Crystal Structures of Three New Copper(II) Halide Layered Perovskites: Structural, Crystallographic, and Magnetic Correlations. *J. Am. Chem. Soc.* **1988**, *110*, 8639.
(34) Stoumpos, C. C.; Cao, D. H.; Clark, D. J.; Young, J.; Rondinelli, J. M.; Jang, J. I.; Hupp, J. T.; Kanatzidis, M. G. Ruddlesden−Popper Hybrid Lead Iodide Perovskite 2D Homologous Semiconductors. *Chem. Mater.* **2016**, *28*, 2852.
(35) Tsai, H.; Nie, W.; Blancon, J.-C.; Stoumpos, C. C.; Asadpour, R.; Harutyunyan, B.; Neukirch, A. J.; Verduzco, R.; Crochet, J. J.; Tretiak, S.; Pedesseau, L.; Even, J.; Alam, M. A.; Gupta, G.; Lou, J.; Ajayan, P. M.; Bedzyk, M. J.; Kanatzidis, M. G.; Mohite, A. D. High-efficiency two-dimensional Ruddlesden−Popper perovskite solar cells. *Nature* **2016**, *536*, 312.
(36) Safdari, M.; Svensson, P. H.; Hoang, M. T.; Oh, I.; Kloo, L.; Gardner, J. M. Layered 2D alkyldiammonium lead iodide perovskites: synthesis, characterization, and use in solar cells. *J. Mater. Chem. A* **2016**, *4*, 15638.
(37) Stoumpos, C. C.; Soe, C. M. M.; Tsai, H.; Nie, W.; Blancon, J.-C.; Cao, D. H.; Liu, F.; Traoré, B.; Katan, C.; Even, J.; Mohite, A. D.; Kanatzidis, M. G. High Members of the 2D Ruddlesden-Popper Halide Perovskites: Synthesis, Optical Properties, and Solar Cells of $(CH_3(CH_2)_3NH_3)_2(CH_3NH_3)_4Pb_5I_{16}$. *Chem.* **2017**, *2*, 427.
(38) Cao, D. H.; Stoumpos, C. C.; Yokoyama, T.; Logsdon, J. L.; Song, T.-B.; Farha, O. K.; Wasielewski, M. R.; Hupp, J. T.; Kanatzidis, M. G. Thin Films and Solar Cells Based on Semiconducting Two-Dimensional Ruddlesden−Popper $(CH_3(CH_2)_3NH_3)_2(CH_3NH_3)_{n-1}Sn_nI$. *ACS Energy Lett.* **2017**, *2*, 982.
(39) Wang, Z.; Ganose, A. M.; Niu, C.; Scanlon, D. O. First-principles insights into tin-based two-dimensional hybrid halide perovskites for photovoltaics. *J. Mater. Chem. A* **2018**, *6*, 5652.
(40) Kuroda-Sowa, T.; Horino, T.; Yamamoto, M.; Ohno, Y.; Maekawa, M.; Munakata, M. Structural Control of Copper(I) Coordination Polymers: Construction of One-, Two-, and Three-Dimensional Frameworks of Tetrahedral Copper(I) Ions Bridged by Dicyanobenzene Derivatives. *Inorg. Chem.* **1997**, *36*, 6382.
(41) Graham, P. M.; Pike, R. D.; Sabat, M.; Bailey, R. D.; Pennington, W. T. Coordination Polymers of Copper(I) Halides. *Inorg. Chem.* **2000**, *39*, 5121.
(42) Okubo, T.; Tanaka, N.; Kim, K. H.; Yone, H.; Maekawa, M.; Kuroda-Sowa, T. Magnetic and Conducting Properties of New Halide-Bridged Mixed-Valence $Cu^{I}-Cu^{II}$ 1D Coordination Polymers Including a Hexamethylene Dithiocarbamate Ligand. *Inorg. Chem.* **2010**, *49*, 3700.
(43) Li, Q.; Li, S.; Wang, K.; Quan, Z.; Meng, Y.; Zou, B. High-Pressure Study of Perovskite-Like Organometal Halide: Band-Gap Narrowing and Structural Evolution of $[NH_3\text{-}(CH_2)_4\text{-}NH_3]CuCl_4$. *J. Phys. Chem. Lett.* **2017**, *8*, 500.
(44) Cortecchia, D.; Dewi, H. A.; Yin, J.; Bruno, A.; Chen, S.; Baikie, T.; Boix, P. P.; Grätzel, M.; Mhaisalkar, S.; Soci, C.; Mathews, N. Lead-Free $MA_2CuCl_xBr_{4-x}$ Hybrid Perovskites. *Inorg. Chem.* **2016**, *55*, 1044.
(45) Cortecchia, D.; Soci, C.; Cametti, M.; Petrozza, A.; Martí-Rujas, J. Crystal Engineering of a Two-Dimensional Lead-Free Perovskite with Functional Organic Cations by Second- Sphere Coordination. *ChemPlusChem* **2017**, *82*, 671.
(46) Ito, S.; Murakami, T. N.; Comte, P.; Liska, P.; Grätzel, C.; Nazeeruddin, M. K.; Grätzel, M. Fabrication of thin film dye sensitized solar cells with solar to electric power conversion efficiency over 10%. *Thin Solid Films* **2008**, *516*, 4613.
(47) Kim, H.-S.; Lee, C.-R.; Im, J.-H.; Lee, K.-B.; Moehl, T.; Marchioro, A.; Moon, S.-J.; Humphry-Baker, R.; Yum, J.-H.; Moser, J.

DOI: 10.1021/acsaem.8b02134
ACS Appl. Energy Mater. 2019, 2, 2178−2187

E.; Grätzel, M.; Park, N.-G. Lead iodide perovskite sensitized all-solid-state submicron thin film mesoscopic solar cell with efficiency exceeding 9%. *Sci. Rep.* **2012**, *2*, 591.
(48) Chusuei, C. C.; Brookshier, M. A.; Goodman, D. W. Correlation of Relative X-ray Photoelectron Spectroscopy Shake-up Intensity with CuO Particle Size. *Langmuir* **1999**, *15*, 2806.
(49) Schlaf, R.; Murata, H.; Kafafi, Z. Work function measurements on indium tin oxide films. *J. Electron Spectrosc. Relat. Phenom.* **2001**, *120*, 149.
(50) Schulz, P.; Edri, E.; Kirmayer, S.; Hodes, G.; Cahen, D.; Kahn, A. Interface energetics in organo-metal halide perovskite-based photovoltaic cells. *Energy Environ. Sci.* **2014**, *7*, 1377.
(51) Chilvery, A. K.; Guggilla, P.; Batra, A. K.; Gaikwad, D. D.; Currie, J. R. Efficient planar perovskite solar cell by spray and brush solution-processing methods. *J. Photonics Energy* **2015**, *5*, 053093.
(52) Dualeh, A.; Moehl, T.; Tétreault, N.; Teuscher, J.; Gao, P.; Nazeeruddin, M. K.; Grätzel, M. Impedance Spectroscopic Analysis of Lead Iodide Perovskite-Sensitized Solid-State Solar Cells. *ACS Nano* **2014**, *8*, 362.
(53) Gelderman, K.; Lee, L.; Donne, S. W. Flat-Band Potential of a Semiconductor: Using the Mott−Schottky Equation. *J. Chem. Educ.* **2007**, *84*, 685.
(54) Lin, Q.; Armin, A.; Nagiri, R. C. R.; Burn, P. L.; Meredith, P. Electro-optics of perovskite solar cells. *Nat. Photonics* **2015**, *9*, 106.
(55) Bard, A. J.; Faulkner, L. R. *Electrochemical Methods: Fundamentals and Applications*, 2nd ed.; John Wiley & Sons, Inc.: New York, 2001.
(56) Vetter, M.; Schwuchow, A.; Andrä, G. Photoluminescence at room temperature of liquid-phase crystallized silicon on glass. *AIP Adv.* **2016**, *6*, 125004.
(57) Yan, J.; Ke, X.; Chen, Y.; Zhang, A.; Zhang, B. Effect of modulating the molar ratio of organic to inorganic content on morphology, optical absorption and photoluminescence of perovskite. *Appl. Surf. Sci.* **2015**, *351*, 1191.
(58) Lichty, D. M. The solubility of the chloride, the bromide, and the iodide of lead, in water, at temperatures from 0° upward. *J. Am. Chem. Soc.* **1903**, *25*, 469.

DOI: 10.1021/acsaem.8b02134
ACS Appl. Energy Mater. 2019, 2, 2178−2187